

1



2 Prediction Of Geospace Radiation Environment and Solar wind
3 parameters

4

5 Work Package 6

6 Forecast of the radiation belt environment

7

8 Deliverable D6.2

9 Data assimilation extension for VERB

10

11 Tatyana Podladchikova¹ and Yuri Shprits²

12

1/23/2017

13

1. Skolkovo Institute of Science and Technology, Moscow, Russia

14

2. Helmholtz Centre Potsdam, GFZ German Research Centre for Geosciences,
15 Potsdam, Germany

16

17

This project has received funding from the European Union's Horizon 2020 research and innovation programme under grant agreement No
18 637302

19



1

2

3 **Introduction**

4 Assimilation of observations of electron fluxes in the radiation belts is needed for
5 the understanding and forecasting of physical processes in the radiation belts, and the prediction
6 and mitigation of space weather effects in the hazardous space environment. Over a period of less
7 than 10 years, there has been steady increase in Kalman filter applications to solve
8 the assimilation problem of satellite observations. However, a fundamental problem in
9 the application of Kalman filter is the assumption about values of the noise statistics that describe
10 the model errors arising from the imperfect description of the process dynamics. Additional
11 difficulties appear in the assimilation of multiple-satellite observations characterized by a large
12 variety of unknown observation error statistics. The effectiveness of estimation and forecasting of
13 radiation belts dynamics depends on how well the dominant physics is described by the model and
14 the accuracy of the unknown noise statistics. However, accurate parameter estimation is a
15 challenging problem for the case of sparse satellite observations and high variability of radiation
16 belts dynamics. This explains why the application of a Kalman filter with an empirical choice of
17 noise statistics that is not sufficiently justified may significantly distort the assimilation output and
18 provide false conclusions about the dynamics of radiation belts. Therefore, the development of
19 consistent identification methods for physical model errors and satellites observation errors, and
20 the construction of an adaptive Kalman filter on the basis of parameter identification that optimizes
21 the assimilation output are of prime importance for the estimation and prediction of radiation belts
22 dynamics.

23 In this study, we develop a new generation of assimilation models by combining the
24 observations from multiple international scientific satellites with the state of art physical-based
25 models to provide global reconstruction of energetic electron fluxes in the inner magnetosphere
26 and operational forecasting of space weather conditions in the near-Earth environment. We focus
27 on the development of consistent identification methods for unknown noise statistics such as the
28 bias and covariance matrix of model errors that characterize the uncertainty in the dynamics of the
29 radiation belts. We present the further improvement of data assimilation developing the
30 identification technique to estimate the observation errors statistics that is crucially important for
31 the optimal assimilation output. We identify the coefficients of proportionality characterizing the
32 dependence of observation errors for satellite observations. Additional improvement and the
33 accuracy increase of assimilation of the electron radiation belts observations is developed by the
34 implementation of the backward optimal smoothing procedure applied to the forward Kalman filter
35 estimates providing further refinement in our knowledge of the key physical mechanisms and
36 leading to the operational forecasting of radiation belts.

37 **1. The state-space model construction for 3-D data assimilation**

38 The evolution of relativistic electrons in the Earth's radiation belts can be described by the 3-
39 D modified Fokker-Planck equation [Schulz and Lanzerotti,1974] in terms of the adiabatic
40 invariants that includes radial, pitch angle, and energy diffusion

$$41 \quad \frac{\partial f}{\partial t} = L^{*2} \frac{\partial}{\partial L^*} |_{\mu,J} \frac{1}{L^{*2}} D_{L^*,L^*} \frac{\partial f}{\partial L^*} |_{\mu,J} + \frac{1}{p^2} \frac{\partial}{\partial p} |_{\alpha_0,L} p^2 D_{pp} \frac{\partial}{\partial p} |_{\alpha_0,L} +$$

$$+ \frac{1}{T(\alpha_0) \sin(2\alpha_0)} \frac{\partial}{\partial \alpha_0} |_{p,L} T(\alpha_0) \sin(2\alpha_0) D_{\alpha_0 \alpha_0} \frac{\partial}{\partial \alpha_0} |_{p,L} - \frac{f}{\tau}$$

Here D_{L^*,L^*} , D_{pp} , $D_{\alpha_0 \alpha_0}$ are the radial, momentum, and pitch angle diffusion coefficients, respectively. The lifetime parameter τ accounts for losses of particles inside the loss cone due to collisions with atmospheric neutrals, T is a function of α in a dipole field. Quasi-linear diffusion coefficients as inputs for the VERB code are computed with the 3-D Versatile Electron Radiation Belt Code (VERB), that is capable of computing resonance scattering rates, including first-order, Landau, and higher-order resonant scattering by obliquely propagating waves. To compute radial transport, we use the magnetic radial diffusion rates of Brautigam and Albert [2000].

The numerical solution of 3-D Fokker-Plank equation X_j^{mod} at every step j is determined on the basis of 3-D VERB code and split operator approach in which the multidimensional solution S_j is divided into three operators that are solved sequentially. The split operator technique is schematically presented in Figure 1. The obtained solution S_j is linearly interpolated on the invariant coordinates of the model (L^*, μ, α), the size of the model grid is 51 steps in the L^* direction, 51 steps in the μ direction, and 18 steps in the α direction. The L^* grid is defined from 1 RE to 6 RE, the μ grid is defined by a minimum energy of 0.01 MeV and a maximum energy of 10 MeV at the outer radial boundary of $L^* = 6$, and the pitch angle is defined from 0.7° to 89.7° .

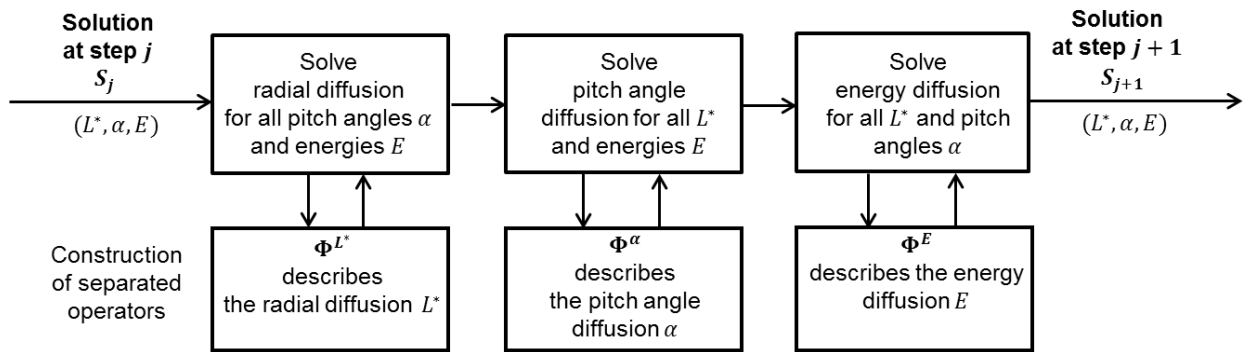


Figure 1. The split operator scheme

To apply a Kalman filter it is necessary to present the physical model of dynamics of Earth's radiation belts in state space by constructing the dependence of the future state of the dynamical system on its present state.

The state equation for fixed values of μ and α is given by

$$X_{j+1} = \Phi_{j+1,j} X_j + W_{j+1} \Delta t_{j+1}, \quad j = 1, \dots, N \quad (1)$$

where X_j is a 51 – dimensional state vector at step j , whose components are electron phase space densities (PSD) for all values of L^* at fixed values of μ and α ; $\Phi_{j+1,j}$ is a 51×51 –dimensional transition matrix, that relates the current state vector X_j at step j with the state vector X_{j+1} at step $j + 1$, Δt_{j+1} represents time interval between measurements, and W_{j+1} is an uncorrelated model noise that describes the errors of theoretical model of radiation belts.

The measurement equation for fixed values of μ and α is given by

$$Z_j = H_j X_j + Y_j \quad (2)$$

1 Here Z_j is a p – dimensional measurement vector at step j , which components are values
2 of PSD obtained from measured electron fluxes using Tsyganenko model TS04 for the calculation
3 of the third invariant and interpolated onto the multidimensional grid (L^*, μ, α) in terms of adiabatic
4 invariants; H_j is the $p \times 51$ – dimensional observation matrix that translates the state vector X_j to
5 the measurement vector Z_j , size of p depends on number of available measurements at the current
6 time step j ; Y_j is an uncorrelated unbiased measurement noise that describes the PSD observation
7 errors conditioned by the errors of electron flux measurements and the errors of PSD calculation
8 from measured fluxes. Statistical characteristics of model noise W_i and measurement noise Y_j are
9 unknown and have to be identified to provide best estimation of unknown system state.

10 The knowledge of separate transition matrices for the split operator method : Φ^{L^*} , Φ^α and Φ^E
11 doesn't allow us to directly determine the transition matrix $\Phi_{j+1,j}$ for 3-D model that relates state
12 vectors X_j and X_{j+1} . In order to reconstruct the transition matrix $\Phi_{j+1,j}$ we use the obtained
13 solutions S_j on the grid (L^*, μ, α) by successively fixing every value of pitch-angles α and energies
14 E on the grid and define the transition matrix in the following way

$$15 \quad \Phi_{j+1,j} = \text{diag}\left(\frac{S_{j+1}}{S_j}\right)$$

16 The reconstructed matrices have diagonal form that allowed us to avoid the computational
17 difficulties related with ill-conditioned matrices of estimation errors, and to perform the
18 independent filtration of PSD observations at each L^* by fixing successively every value of pitch-
19 angles α and energies E on the (L^*, μ, α) grid.

20

21 **2. Noise statistics identification: model and measurement errors**

22 In practice, model errors and characteristics of satellite observations are poorly known, which
23 may cause the failure of a Kalman filter algorithm and false conclusions about the radiation belt
24 dynamics. Correct specification of the model and measurement error statistics is necessary for the
25 development of the next generation of radiation belt specification models providing the effective
26 PSD reconstruction and hence the prediction and mitigation of space weather effects in the
27 hazardous space environment. Estimate of model errors also allows us to determine the model
28 accuracy which is usually requested by stakeholders to understand the accuracy of model
29 predictions and estimate prediction confidence levels. Estimation of observational errors can help
30 accurately assimilate data.

31 This report describes the development of a technique to identify statistical characteristics of
32 model and measurement noise for 3-D model including radial, pitch angle, and energy diffusion
33 that is based on the same principles, but is significantly simpler for independent assimilation of
34 measurements for every L^* using the one-dimensional model at state space

$$35 \quad \begin{aligned} x_{j+1} &= \phi_{j+1,j} x_j + w_{j+1} \Delta t_{j+1} \\ z_j &= x_j + \varepsilon_j \end{aligned} \quad (3)$$

36 where x_j is a value of PSD at the considered L^* at fixed values of pitch-angle α and energy E at
37 step j , $\phi_{j+1,j}$ is the diagonal element of transition matrix $\Phi_{j+1,j}$ corresponding to the given L^* ,
38 w_{j+1} is the uncorrelated noise with unknown bias q and variance σ_w^2 , Δt_{j+1} is time interval
39 between PSD observations at steps j and $j + 1$,⁴ and ε_j is uncorrelated unbiased measurement noise
40 with unknown variance σ_ε^2 .

1

2 **2.1. The identification of model noise bias**

3 The key principle to identify the unknown error statistics lies in the construction
 4 of residuals characterizing the mismatch between an observation and an auxiliary estimate
 5 of the state vector. We construct the following residuals

6
$$v_j = z_j - \phi_{j,j-1}z_{j-1}, \quad j = 2,3, \dots \quad (4)$$

7 where z_j is the available measurement at step j at the considered L^* , $\phi_{j,j-1}z_{j-1}$ is the uncorrelated
 8 sequence of auxiliary estimates of state vector component x_j made only by using one measurement
 9 z_{j-1} at step $j - 1$. This estimate is equivalent to that of a Kalman filter with minimal memory for
 10 a dynamical system free from noises. We will further show that the residual v_j can be presented in
 11 the form of an explicit linear function of unobserved model and measurement noise terms w_{j+1} and
 12 ε_j of the model given by Equation (3).

13 Substituting the measurement equation given by Equation (3) for z_j and z_{j-1} in Equation (4)
 14 the residual v_j can be presented in the following way

15
$$v_j = x_j + \varepsilon_j - \phi_{j,j-1}x_{j-1} - \phi_{j,j-1}\varepsilon_{j-1} \quad (5)$$

16 Let us substitute the state equation given by Equation (3) for x_j in Equation (5)

17
$$v_j = w_j \Delta t_j + \varepsilon_j - \phi_{j,j-1}\varepsilon_{j-1} \quad (6)$$

18 As it is seen from Equation (6) the known residual v_j has a linear dependence on the model
 19 and measurement noise w_j and ε_j and does not contain a state vector component x_j on the right
 20 hand side.

21 The next step is to find the mathematical expectation of the left and right sides of Equation (6).
 22 Taking into account that mathematical expectation $E[w_j] = q$ and measurement noise ε_j is
 23 assumed to be unbiased, we obtain the following equality

24
$$E[v_j] = q\Delta t_j \quad (7)$$

25 Thus, the residuals v_j can be presented as

26
$$v_j = q\Delta t_j + \eta_j$$

27 where η_j is an unbiased random noise $E[\eta_j] = 0$.

28 Then

29

$$\frac{1}{N-1} \sum_{j=2}^N v_j = q \frac{1}{N-1} \sum_{j=2}^N \Delta t_j + \frac{1}{N-1} \sum_{j=2}^N \eta_j \quad (8)$$

30

31 The term $\frac{1}{N-1} \sum_{j=2}^N \eta_j$ in Equation (8) approaches its mathematical expectation $E[\eta_j] = 0$ when
 32 $N \rightarrow \infty$ because η_j and η_{j+l} are independent when $j > 1$ that is conditioned by the construction
 33 of residuals v_j .

34 Thus the estimate of model noise bias q is determined form the Equation (8)

$$\hat{q} = \frac{1}{N-1} \sum_{j=2}^N v_j \Big/ \frac{1}{N-1} \sum_{j=2}^N \Delta t_j \quad 5 \quad (9)$$

1 where N is the number of residuals v_j .

2

3 **2.2. The identification of model noise variance**

4 As the model noise bias q is already determined on the basis of Equation (9), let us consider
5 the squared centered residuals $v_j - \hat{q}$ using Equation (6)

$$6 \quad (v_j - \hat{q})^2 = ((w_j - \hat{q})\Delta t_j + \varepsilon_j - \phi_{j,j-1}\varepsilon_{j-1})^2 \quad (10)$$

7 Taking into account that noises $w_j - \hat{q}$ and ε_j are independent white noise sequences,
8 the mathematical expectation of both sides of Equation (10) is given by

$$9 \quad E[(v_j - \hat{q})^2] = \sigma_w^2 \Delta t_j^2 + \sigma_{\varepsilon_j}^2 + \phi_{j,j-1}^2 \sigma_{\varepsilon_{j-1}}^2$$

10 Thus, the squared centered residuals $(v_j - \hat{q})^2$ can be presented as

$$11 \quad (v_j - \hat{q})^2 = \sigma_w^2 \Delta t_j^2 + \sigma_{\varepsilon_j}^2 + \phi_{j,j-1}^2 \sigma_{\varepsilon_{j-1}}^2 + \zeta_j \quad (11)$$

12 where ζ_j is a random noise term with the mathematical expectation $E[\zeta_j] = 0$.

13 As follows from Equation (11), the estimate of the mathematical expectation of the squared
14 centered residuals is given by

$$\frac{1}{N-1} \sum_{j=2}^N (v_j - \hat{q})^2 = \frac{1}{N-1} \sigma_w^2 \sum_{j=2}^N \Delta t_j^2 + \frac{1}{N-1} \sum_{j=2}^N (\sigma_{\varepsilon_j}^2 + \phi_{j,j-1}^2 \sigma_{\varepsilon_{j-1}}^2) + \frac{1}{N-1} \sum_{j=2}^N \zeta_j \quad (12)$$

The term $\frac{1}{N-1} \sum_{j=2}^N \zeta_j$ in Equation (12) approaches its mathematical expectation $E[\zeta_j] = 0$

15 when $N \rightarrow \infty$ because ζ_j and ζ_{j+l} are independent when $l > 1$.

16 In papers dedicated to the assimilation of PSD observations, an assumption that model and
17 measurement errors are defined by a certain percentage of observations is often used. We assume
18 that the variance $\sigma_{\varepsilon_j}^2$ can be presented as $(\lambda z_j)^2$, where λ are unknown coefficients to be identified
19 on the basis of satellite measurements. Therefore, Equation (12) can be written as

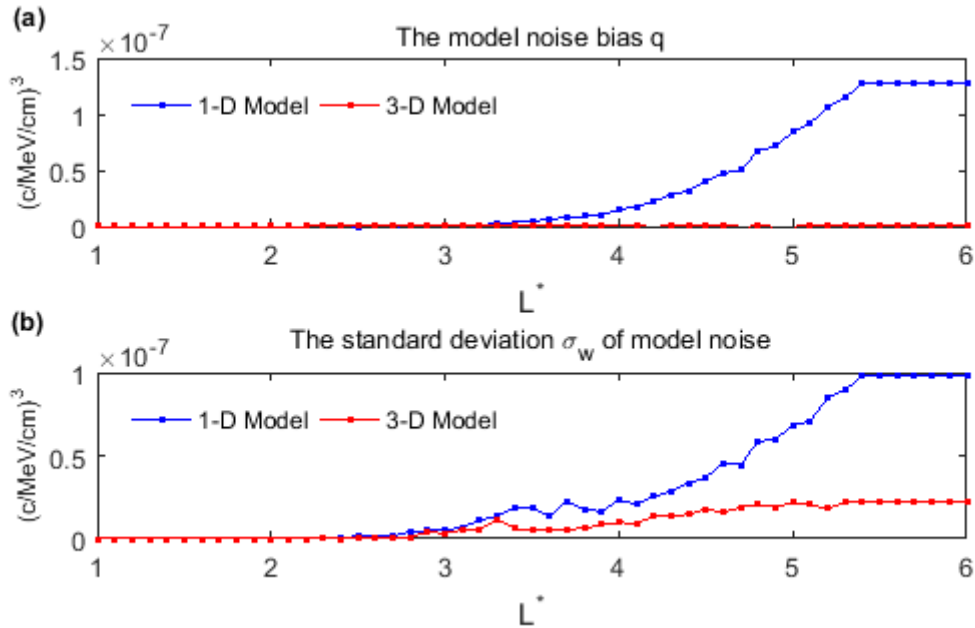
$$\sum_{j=2}^N (v_j - \hat{q})^2 = \sigma_w^2 \sum_{j=2}^N \Delta t_j^2 + \lambda^2 \sum_{j=2}^N (z_j^2 + \phi_{j,j-1}^2 z_{j-1}^2) \quad (13)$$

20 Equation (13) is a linear equation with two unknown values σ_w^2 and λ^2 . The peculiarity
21 of Equation (13) lies in the fact that the number of available PSD observations is significantly
22 smaller than the total number of L^* bins where the error caused by model noise is accumulated.
23 The main contribution to the right part of Equation (13) is made by first term containing
24 the model noise variance σ_w^2 when the interval between measurements Δt_j is significant and is
25 greater than 20 steps, for example. In this case second term containing the measurement noise is
26 small compared to the first one because it does not depend on Δt_j . Therefore, we determine
27 the model noise variance σ_w^2 neglecting the second term in the right part of Equation (13)
28 when $\Delta t_j > 20$ in the following way

$$\hat{\sigma}_w^2 = \sum_{j=2}^N (v_j - \hat{q}) / \sum_{j=2}^N (\Delta t_j)^2 \quad (14)$$

29 The identification of model noise bias q and variance σ_w^2 according to the developed algorithm
30 was performed for all values of pitch-angles α and energies E on the grid (L^*, μ, α) using PSD

1 observations obtained from measured electron fluxes by the Van Allen Probes REPT and MagEIS
 2 instruments. Figure 2 shows the estimates of bias q (a) and standard deviation σ_w (b) for L^* from
 3 1 to 6 using REPT Van Allen Probes measurements at fixed values of the adiabatic invariant $\mu =$
 4 2129 MeV/G and pitch angle $\alpha = 43^\circ$ for 3-D model that includes radial, energy, and pitch angle
 5 diffusion (red). For comparison the figure also contains the identification results of bias q (a) and
 6 standard deviation σ_w (b) for 1-D radial diffusion (blue).



7
 8 **Figure 2.** The identification results of model noise statistics for L^* from 1 to 6 using PSD
 9 observations obtained from measured electron fluxes by REPT instrument of Van Allen Probes
 10 A satellite at fixed values of the adiabatic invariant $\mu = 2129$ MeV/G and pitch angle $\alpha = 43^\circ$
 11 for 3-D model (red) that includes radial, energy, and pitch angle diffusion, and 1-D radial
 12 diffusion model (blue). (a) The identified bias \hat{q} of model noise w over one step (10 min). (b)
 13 The identified standard deviation $\hat{\sigma}_w^2$ of model noise w over one step.

14
 15 As shown in Figure 2a, the model noise bias q for 1-D model (blue) increases with increasing L^* ,
 16 while the transition to a 3-D model allows us to remove this bias (red). Figure 2b shows that the
 17 model noise standard deviation σ_w for 1-D radial diffusion model (blue) increases with the
 18 increase of L^* to the values that are 3-4 times greater than that for 3-D model including radial,
 19 energy, and pitch angle diffusion (red). This is a strong argument in favor of the more accurate 3-
 20 D model compared to a 1-D model that describes only radial diffusion as model noise bias q and
 21 standard deviation σ_w characterize the level of model adequacy. The smaller the values of q and
 22 σ_w , the greater the confidence that the physical model accurately describes the state and evolution
 23 of radiation belts. The proposed approach can also be used to test different model parameters and
 24 diffusion coefficients.

25
 26 **2.3. The identification of measurement noise variance**

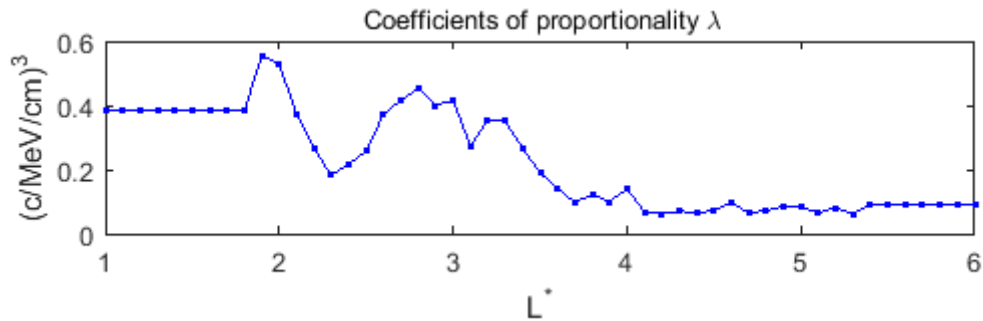
27 To identify the measurement noise variance σ_ε^2 we create the residuals, in which the weight of
 28 measurement noise ε describing observation errors is maximized, while that of model noise W

1 representing model errors is insignificant. It can be achieved when the interval between
 2 measurements is minimal, $\Delta t_j = 1$. During this interval the temporal evolution of PSD should
 3 change insignificantly, resulting in smaller influence of model noise W on Equation (13).
 4 Therefore, we determine the coefficient of proportionality λ^2 and the measurement noise variance
 5 $\sigma_\varepsilon^2 = (\lambda z_j)^2$ by neglecting the first term in the right hand side of Equation (13) when $\Delta t_j = 1$ in
 6 the following way

$$\lambda = \sqrt{\sum_{j=2}^N (v_j - \hat{q})^2 / \left(\sum_{j=2}^N (z_j^2 + \phi_{jj-1}^2 z_{j-1}^2) \right)} \quad (15)$$

7 The identification results of proportionality coefficients λ are presented in Figure 3.

8



9

10 **Figure 3.** Coefficients of proportionality for standard deviation σ_ε of measurement noise ε , $\sigma_\varepsilon =$
 11 λz_j .

12

13 As shown in Figure 3, coefficients λ decrease with increasing L^* , i.e. the relative error
 14 of measurements decreases as L^* increases. The model estimates obtained and measurement noise
 15 statistics q , σ_w , and σ_ε were used to develop an adaptive Kalman filter for the PSD observations
 16 obtained from measured electron fluxes by REPT and MagEIS instruments.

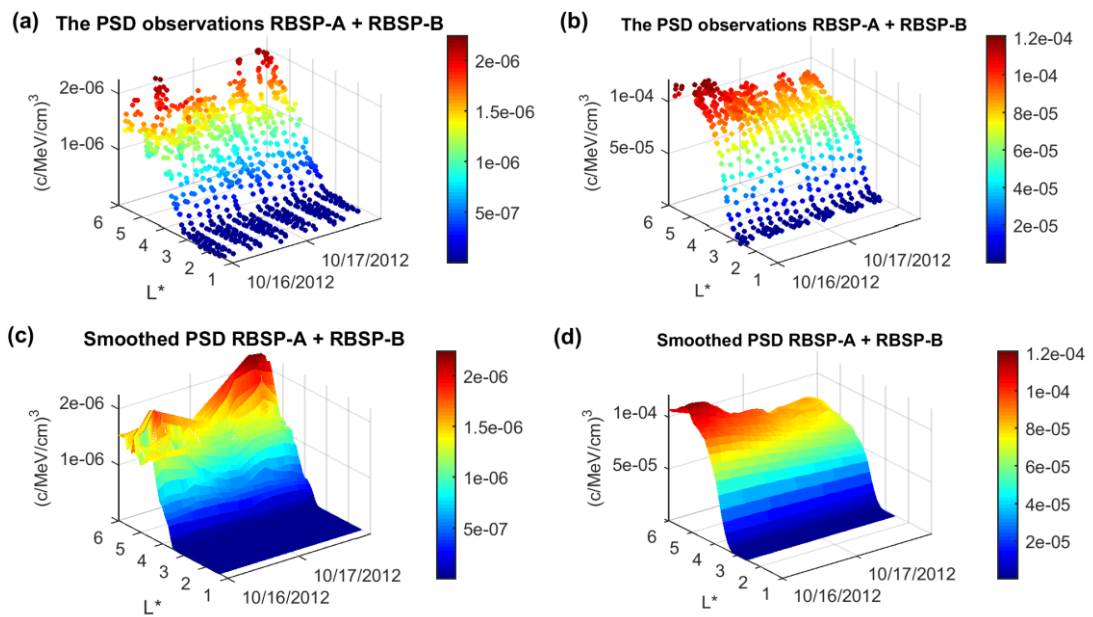
17

18 **3. The 3-D filtration and smoothing of Van Allen Probes data**

19 **3.1. Joint assimilation of final level 3 data obtained from REPT and MagEIS instruments** 20 **of Van Allen Probes A and B satellites**

21 A global reanalysis of the radial profile of electron PSD is performed by joint assimilation of
 22 data from REPT and MagEIS instruments on the Van Allen Probes A and B satellites. The
 23 construction of a state space model and reconstruction of the transition matrix presented in section
 24 1 allowed us to perform an independent assimilation of PSD observations by applying the 1-
 25 dimensional Kalman filter at each L^* by fixing successively every value of pitch-angles α and
 26 energies E on the (L^*, μ, α) grid. The Kalman filter does not completely solve the data assimilation
 27 problem for the past measurements in an optimal way as it uses observation information available
 28 at the current time and does not adjust a data assimilation algorithm by the PSD observations
 29 obtained after the current time. An additional backward smoothing procedure applied to the
 30 forward Kalman filter estimates uses all available PSD observations, including observations after
 31 the current assimilation step, and provides an improved reconstruction of PSD compared to the
 32 Kalman filter [Sage and White, 1977].

1 The results of joint assimilation of MagEIS and REPT data for the full (L^*, μ, α) grid for all
 2 values of L^*, μ , and α over the period October 2012 – April 2013 can be found at
 3 ftp://rbm.epss.ucla.edu/ftpdisk1/3D_Data_Assimilation/v2.0/.
 4 Figure 4a shows the PSD observations obtained from measured electron fluxes by REPT
 5 instrument of both satellites Van Allen Probes A and B at fixed values of $\mu = 2129$ MeV/G and
 6 pitch angle $\alpha = 43^\circ$ over the period of two days in October 16-17, 2012. Figure 4b shows the PSD
 7 observations obtained from measured electron fluxes by MagEIS instrument of A and B satellites
 8 at fixed values of $\mu = 159$ MeV/G and pitch angle $\alpha = 43^\circ$ over the same period. Figures 4c and
 9 4d provide the estimation results of PSD dynamics in the entire magnetosphere within L^* from 1
 10 to 6 by a Kalman filter and smoothing using data obtained by REPT (a) and MagEIS (a)
 11 instruments.



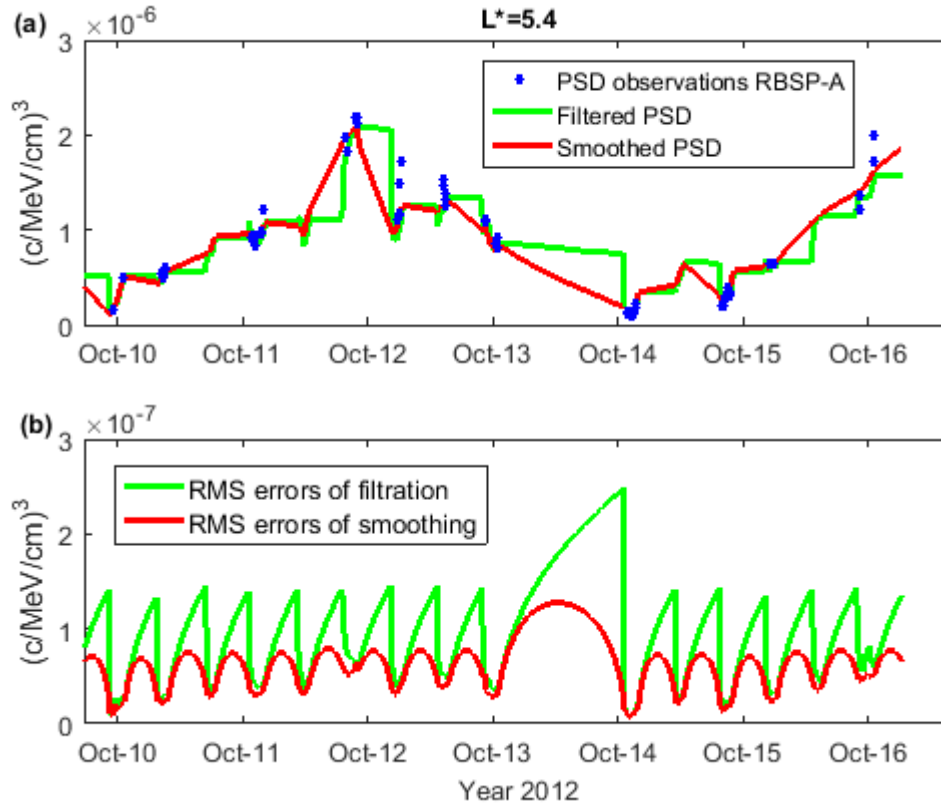
12
 13 **Figure 4.** The reconstructed PSD estimates in the entire magnetosphere within L^* from 1 to 6 by
 14 a Kalman filter and smoothing using measurements of Van Allen Probes A and B satellites. (a)
 15 REPT ten min PSD observations at fixed $\mu = 2129$ MeV/G and pitch angle $\alpha = 43^\circ$. (b)
 16 MagEIS ten min PSD observations at fixed $\mu = 159$ MeV/G and pitch angle $\alpha = 43^\circ$ (c) The
 17 reconstructed PSD using both REPT-A and REPT-B observations (d) The reconstructed PSD
 18 using both MagEIS -A and MagEIS -B observations. X axis shows the time period of
 19 assimilation of two days in October 16-17, 2012. Y axis gives L^* from 1 to 6, and Z axis
 20 provides the PSD observations and the reconstructed PSD estimates.

21
 22 The proposed assimilation technique of satellite measurements provides the filtration
 23 of random fluctuations and fills the gaps at intervals between sparse satellite observations.
 24

25 3.2. Analysis of assimilation accuracy

26 Figure 5a shows the filtered (green) and smoothed (red) PSD estimates at $L^* = 5.4$ at fixed
 27 values of $\mu = 2129$ MeV/G and pitch angle $\alpha = 43^\circ$ over the period of seven days in October 10-
 28 16, 2012. Blue dots show available PSD observations obtained from measured electron fluxes by

1 the Van Allen REPT instrument on satellite A that were used in the assimilation algorithms. Figure
2 5b shows RMS errors of filtration (green) and smoothing (red) determined as root squares of
3 diagonal elements of the filtration and smoothing error covariance matrices provided by Kalman
4 filter and smoothing algorithms at $L^* = 5.4$.

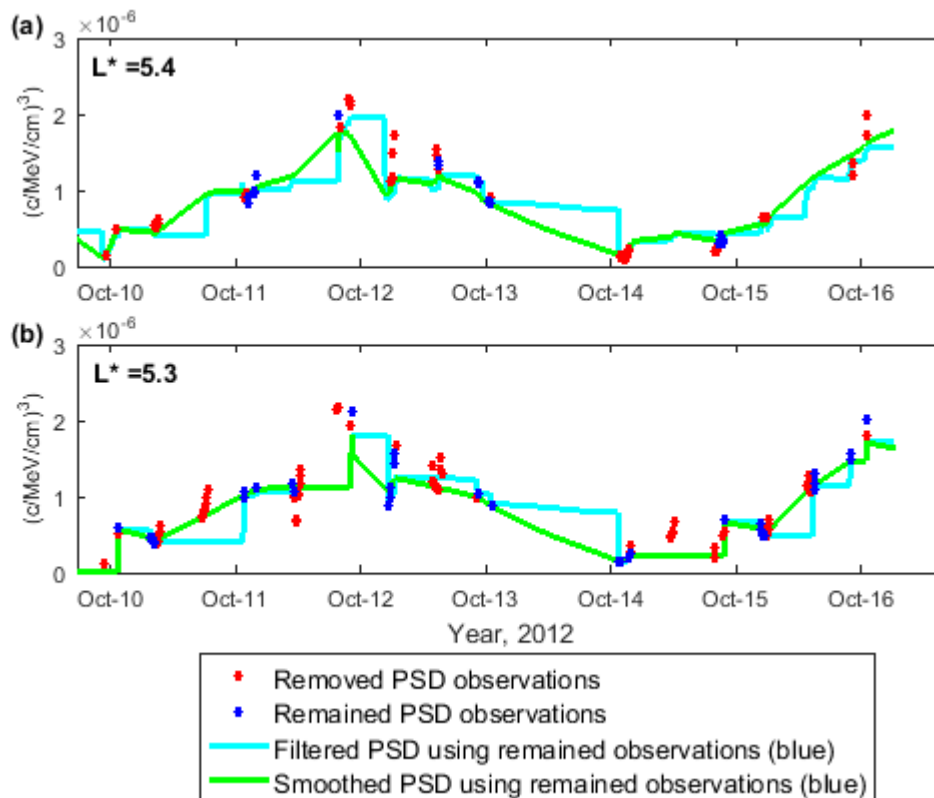


5
6 **Figure 5.** Results of PSD reconstruction at $L^* = 5.4$ at fixed values of $\mu = 2129$ MeV/G and pitch
7 angle $\alpha = 43^\circ$ over the period of seven days in October 10-16, 2012. (a) Blue dots - PSD
8 observations obtained from measured electron fluxes by REPT instrument of Van Allen Probes A
9 satellite that were used in the assimilation algorithms. Green line – filtered PSD estimates. Red
10 line – smoothed PSD estimates. (b) RMS errors of filtration (green) and smoothing (red)
11 determined as root squares of diagonal elements of the filtration and smoothing error covariance
12 matrices provided by Kalman filter and smoothing algorithms.

13
14 As shown in Figure 5b, the dynamics of the filtration and smoothing errors is characterized by
15 cyclic behavior. The RMS errors become minimal during periods in which the PSD observations
16 are available. Within data gaps the RMS errors increase by an amount that depends on the length
17 of the gap. However, the smoothed PSD estimates demonstrate the increased accuracy of global
18 reconstruction compared to the Kalman filter estimates. This is of particular importance to produce
19 an objective reanalysis of the sparse satellite observations.

20 To further analyze the effectiveness of smoothing for the global reconstruction of the dynamics
21 of radiation belts compared to Kalman filter, additional tests are performed. Figure 6 shows the
22 filtered and smoothed PSD estimates at $L^* = 5.4$ (a) and $L^* = 5.3$ (b) at fixed values of $\mu = 2129$
23 MeV/G and pitch angle $\alpha = 43^\circ$ over the period of seven days in October 10-16, 2012. The red
24 and blue dots show the available PSD observations obtained from measured electron fluxes by

1 REPT instrument of Van Allen Probes A satellite. To test the robustness of our method we exclude
 2 12 points from every 18 points available. Assimilation with remaining points produces similar
 3 results. The red dots were removed from the reanalysis and are not used for the filtration and
 4 smoothing. Filtration (cyan) and smoothing (green) of data was performed only by using remained
 5 PSD observations (blue dots).



6
 7 **Figure 6.** The filtered and smoothed PSD estimates at $L^* = 5.4$ (a) and $L^* = 5.3$ (b) at fixed values
 8 of $\mu = 2129$ MeV/G and pitch angle $\alpha = 43^\circ$ over the period of seven days in October 10-16,
 9 2012. Red dots - removed PSD observations obtained from measured electron fluxes by REPT
 10 instrument of Van Allen Probes A satellite not participating in the filtration and smoothing. From
 11 every 18 points, 12 points were excluded from the data assimilation (67% of gaps). Blue dots -
 12 remained PSD observations used for the filtration and smoothing. Cyan line - filtered PSD
 13 estimates using remained observations (blue dots). Green line - smoothed PSD estimated using
 14 remained observations (blue dots).

15
 16 The sum of squared deviation between filtered PSD and observations that did not participate in the
 17 data assimilation is 2.4×10^{-12} at $L^* = 5.4$ and 9.4×10^{-12} at $L^* = 5.3$ during the analyzed period of seven
 18 days. At the same time the sum of the squared deviation between the smoothed PSD and
 19 observations that were not used in the data assimilation is smaller, 1.8×10^{-12} at $L^* = 5.4$ and 5.0×10^{-12}
 20 at $L^* = 5.3$. This is an additional argument in favor of more accurate smoothed PSD estimates
 21 compared to Kalman filter results.

22
 23 **4. Development of technique to estimate the radial and energy diffusion rate from**
 24 **the assimilation of satellite observations**

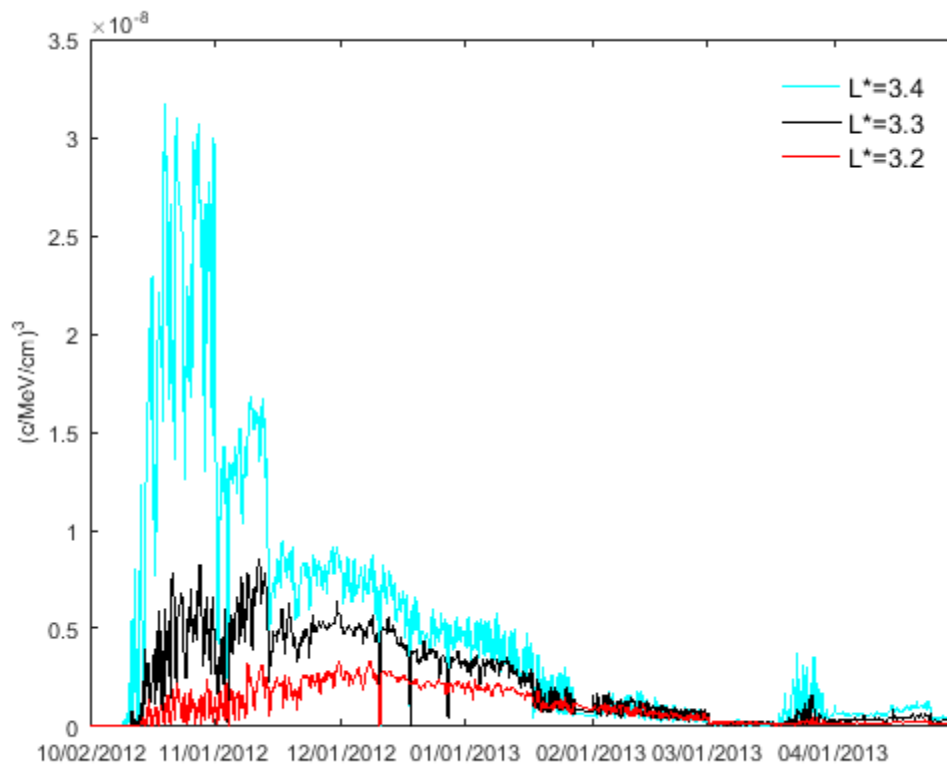
1 The development of adaptive Kalman filter that combines the Van Allen Probes data and 3-D
2 VERB code, its accurate customizations for the reconstruction of the phase space density (PSD)
3 evolution, and the developed identification techniques of model and measurement errors allowed
4 us to reveal physics governing the PSD dynamics and obtain quantitative and qualitative estimates
5 of radial and energy diffusion rates.

6

7 **4.1. The dynamics of phase space density maximum**

8 To estimate the rate of radial and energy diffusion, as well as the direction of their propagation
9 using data assimilation results we analyze the dynamics of the time
10 of maximum PSD at neighboring L^* .

11 Figure 7 shows the reconstructed PSD by a forward Kalman filter and backward smoothing
12 using REPT Van Allen Probes A and B measurements at $L^* = 3.4$ (cyan), $L^* = 3.3$ (black), $L^* =$
13 3.2 (red) at fixed values of $\mu = 2129$ MeV/G and pitch angle $\alpha = 43^\circ$ over the period
14 of seven months in October 2012 – April 2013.



15

16 **Figure 7.** The reconstructed PSD by a Kalman filter and smoothing using REPT Van Allen Probes
17 A and B observations at $L^* = 3.4$ (cyan), $L^* = 3.3$ (black), $L^* = 3.2$ (red) at fixed values of $\mu =$
18 2129 MeV/G and pitch angle $\alpha = 43^\circ$ over the period of seven months
19 in October 2012 – April 2013.

20

21 As shown in Figure 7, the maximum PSD occurs later for lower L^* . However these curves are still
22 characterized by high level of variability. To accurately select the maximum PSD we adjust the
23 obtained PSD estimates by applying an additional forward and backward exponential smoothing
24 [Brown, 1963] for all L^* .

1 Forward exponential smoothing of PSD estimates

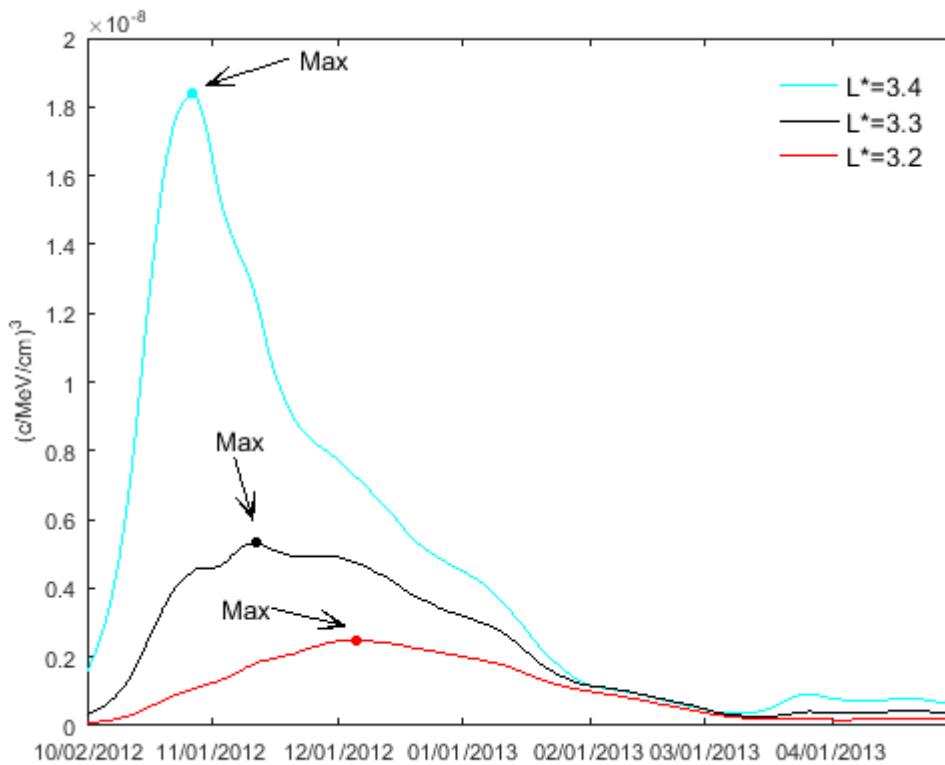
$$2 \quad X_{j+1}^f = X_j^f + \beta(\hat{X}_{j+1} - X_j^f) \quad (16)$$

3 where \hat{X}_{j+1} is the reconstructed PSD estimates and $\beta = 0.001$ is a smoothing coefficient. To
 4 avoid shifting of the estimates X_{j+1}^f we perform their time reversed smoothing

5 Backward exponential smoothing of X_{j+1}^f estimates

$$6 \quad X_k^b = X_{k+1}^b + \beta(X_{k+1}^f - X_{k+1}^b) \quad (17)$$

7 Figure 8 shows the additionally smoothed estimates of PSD X_k^b at $L^* = 3.4$ (cyan), $L^* = 3.3$
 8 (black), $L^* = 3.2$ (red) at fixed values of $\mu = 2129$ MeV/G and pitch angle $\alpha = 43^\circ$ over the
 9 period of seven months between October 2012 – April 2013.



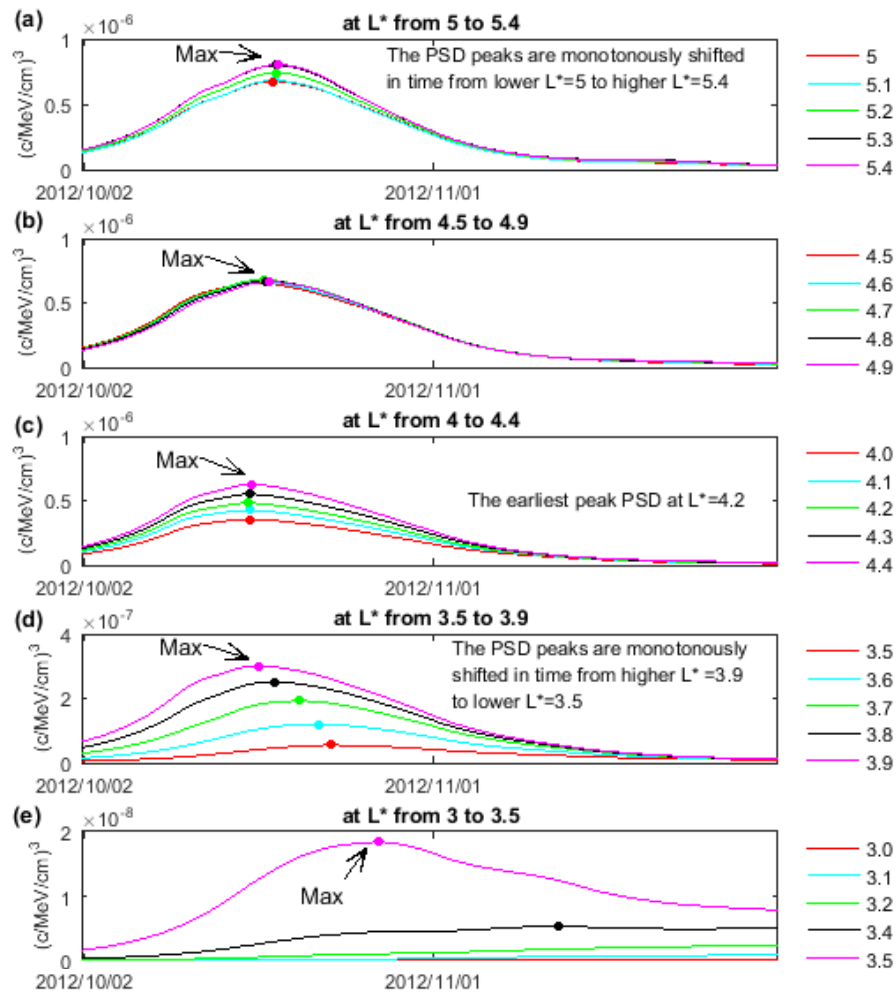
10
 11 **Figure 8.** The additionally smoothed estimates of reconstructed PSD by backward and forward
 12 exponential smoothing at $L^* = 3.4$ (cyan), $L^* = 3.3$ (black), $L^* = 3.2$ (red) at fixed values of $\mu =$
 13 2129 MeV/G and pitch angle $\alpha = 43^\circ$ over the period of seven months between October 2012 –
 14 April 2013.

15
 16 Figure 9 shows the additionally smoothed estimates of reconstructed PSD by backward and
 17 forward exponential smoothing at fixed L^* from 3 to 5.4 at fixed values of $\mu = 2129$ MeV/G and
 18 pitch angle $\alpha = 43^\circ$ over the period of seven months in October 2012 – April 2013.

19 The variation in time at which the maximum in PSD occurred demonstrates the dynamics
 20 of radial diffusion propagation. Analysis of the maximum PSDs as a function of L^* and time
 21 enables the calculation of the rate of radial diffusion. As shown in Figure 9c, the earliest maximum
 22 PSD was observed at $L^* = 4.2$. That indicates¹ that acceleration started locally at this location and

1 then maximum PSD is reached at later times at higher and lower L-shells (Figure 9d) and (Figure
 2 9e).

3 To estimate the main characteristics of radial diffusion we analyze the dependence of time
 4 when the maximum PSD is registered for a particular L^* . Figure 10 shows the dependence of the
 5 registration time of the maximum PSD on L^* from 3.7 to 5.4 at fixed value of pitch angle $\alpha = 43^\circ$
 6 and various values of μ .



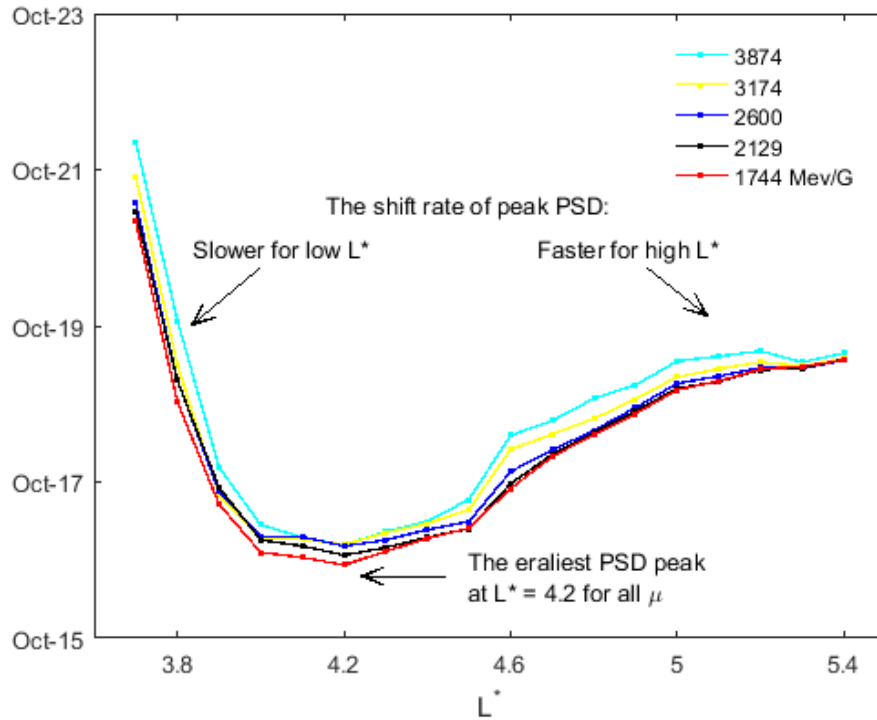
7
 8

9 **Figure 9.** The additionally smoothed estimates of reconstructed PSD by backward and forward
 10 exponential at fixed L^* from 3 to 5.4 at fixed values of $\mu = 2129$ MeV/G and pitch angle $\alpha =$
 11 43° over the period of two months between October 2012 – December 2012.

12

13 As shown in Figure 10, the earliest maximum PSD is registered at $L^* = 4.2$. The maximum
 14 PSD is reached faster at $L^* > 4.2$ compared to lower $L^* < 4.2$ for all adiabatic invariants μ
 15 demonstrating the direction of radial diffusion. Quantitative estimates of the radial diffusion rate
 16 are determined by the shift rate in the maximum PSD relative to L^* . As shown in Figure 10, the
 17 maximum PSD occurs earlier for smaller values of μ confirming the energy diffusion source. For
 18 example, at $L^* = 4.2$ where the earliest maximum PSD was, the electron energy 3.5 MeV
 19 ($\mu = 1744$ MeV/G) increased to values of 5.5 MeV ($\mu = 3874$ MeV/G). The time interval

1 between registration of these maximums for $\mu = 1744$ MeV/G (red) and $\mu = 3874$ MeV/G
 2 (cyan) is 6 hours and 10 minutes that allows us to estimate the diffusion rate 0.32 MeV per hour.
 3



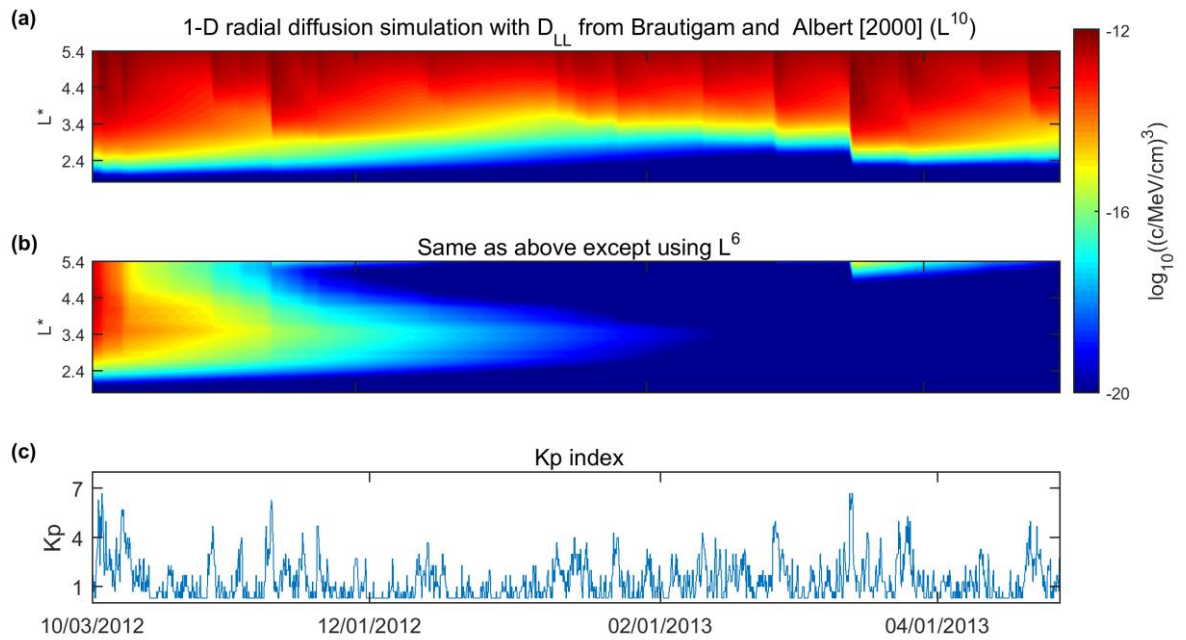
4
 5 **Figure 10.** The dependence of registration time of maximum PSD on L^* from 3.7 to 5.4 at
 6 fixed value of pitch angle $\alpha = 43^\circ$ and various values of μ . X axis shows L^* from 3.7 to 5.4 and
 7 Y axis gives the registration time of maximum PSD.

8
 9 Thus, the assimilation of satellite observations allowed us to infer radial and energy diffusion
 10 rates from observations. The proposed approach can also be used to test different existing models
 11 for radial diffusion coefficients [e.g., Brautigam and Albert, 2000].

12
 13 **4.2. Sensitivity analysis of diffusion rate estimates**

14 In this section, we discuss the influence of a chosen physical model on the estimates of radial
 15 and energy diffusion rate obtained from the data assimilation of satellite observations. We perform
 16 sensitivity tests and demonstrate the power of data assimilation confirming that the estimates of
 17 radial and energy diffusion rate do not almost depend on the chosen model and are obtained from
 18 experimental data. We conduct the sensitivity analysis by varying the power of L, α in the radial
 19 diffusion coefficients $D_{L,L} = 10^{0.506} Kp - 9.325L^\alpha$ [Brautigam and Albert, 2000]. The power of
 20 L in the radial diffusion equation was varied from 6 to 10 and 1-D data assimilation was performed.
 21 The results for $\alpha = 10$ and $\alpha = 6$ are shown in Figures 11 and 12.

22 Figure 11 shows 1-D radial diffusion simulations at fixed $\mu = 2129$ MeV/G and diffusion
 23 coefficient $K = 0.11G^{0.5}RE$ with L^{10} (a) from Brautigam and Albert [2000] and L^6 (b). Kp-index
 24 over the period of seven months between October 2012-April 2013 that was used in the simulation
 25 is shown in Figure 11c.

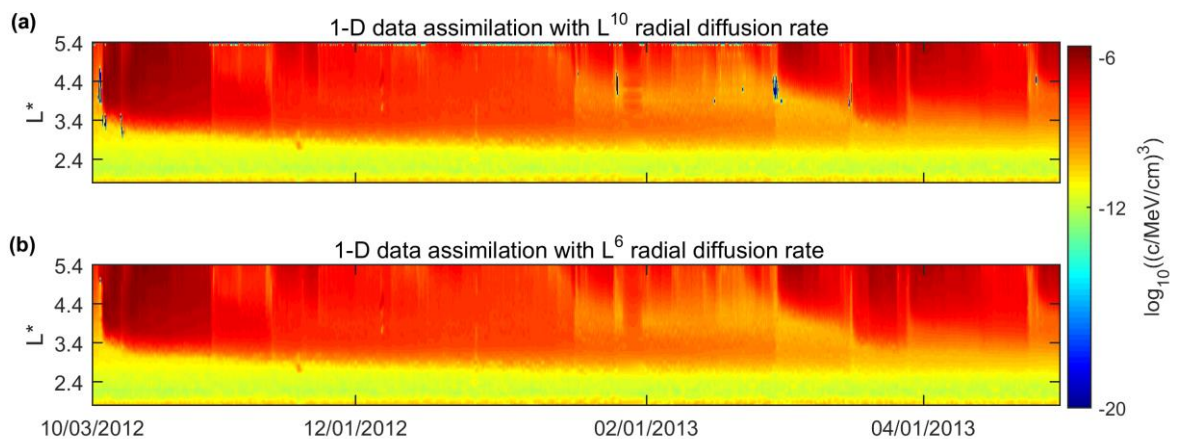


1

2 **Figure 11.** 1-D radial diffusion simulations at fixed $\mu = 2129$ MeV/G and $K = 0.11G^{0.5}RE$. (a)
 3 Simulation utilizing the radial diffusion rates of Brautigam and Albert [2000] (L^{10}). (b)
 4 Simulation using L^6 in place of L^{10} . (c) Kp index.

5

6 The simulation results with different powers of L are vastly different in Figure 11a and 11b.
 7 To determine the error in this case we applied the developed techniques for noise statistics
 8 identification adjusting the physical model and perform the assimilation of Van Allen Probes data
 9 using an adaptive forward Kalman filter followed by a backward smoothing algorithm. The results
 10 of data assimilation for the same period and for each model are shown in Figure 12a and 12b.



11

12 **Figure 12.** The results of data assimilation of Van Allen Probes measurements fixed $\mu = 2129$
 13 MeV/G and $K = 0.11G^{0.5}RE$. (a) Reanalysis with 1-D diffusion based on the radial diffusion
 14 rates of Brautigam and Albert [2000] (L^{10}), (b) Reanalysis with 1-D diffusion using L^6 , in place
 15 of L^{10} .

16

1 As shown in Figure 12, the difference between the two panels (a) and (b) is negligible in this
2 case. This is a demonstration of the fact that if the error statistics are correctly defined, then the
3 estimation results are largely insensitive to the use of an incorrect model. In this case, the data are
4 weighted higher by the Kalman filter gain.

5 Thus, the assimilation results are largely unchanged by the use of different radial diffusion
6 coefficients in cases when reliable noise statistic identification and accurate customization
7 of the assimilation algorithm lead to a good estimate of the true PSD in the system. This is
8 a strong argument that estimates of the diffusion rates may be inferred from the data assimilation
9 and do not depend strongly on the assumptions of the model as there are sufficient data to correct
10 them.

11 The example of a sensitivity test to D_{LL} is important for the proposed method. What is shown
12 is that the results of data assimilation do not depend on the assumed radial diffusion model, and
13 thus our inferred radiation diffusion rates will be driven by data where the model is incorrect, and
14 not by the assumptions of the model.

16 **4.3. Estimation of radial, energy and pitch angle diffusion rate for various values** 17 **of adiabatic invariants μ and α .**

18 The development of techniques to extract the radial, energy and pitch angle diffusion rate from
19 experimental data is important to test different existing models of radial diffusion coefficients [e.g.,
20 Brautigam and Albert, 2000] and incorporate the proper diffusion coefficients into numerical
21 simulations. In this section we focus on the further development of estimation of diffusion rates
22 from assimilation results of satellite observations.

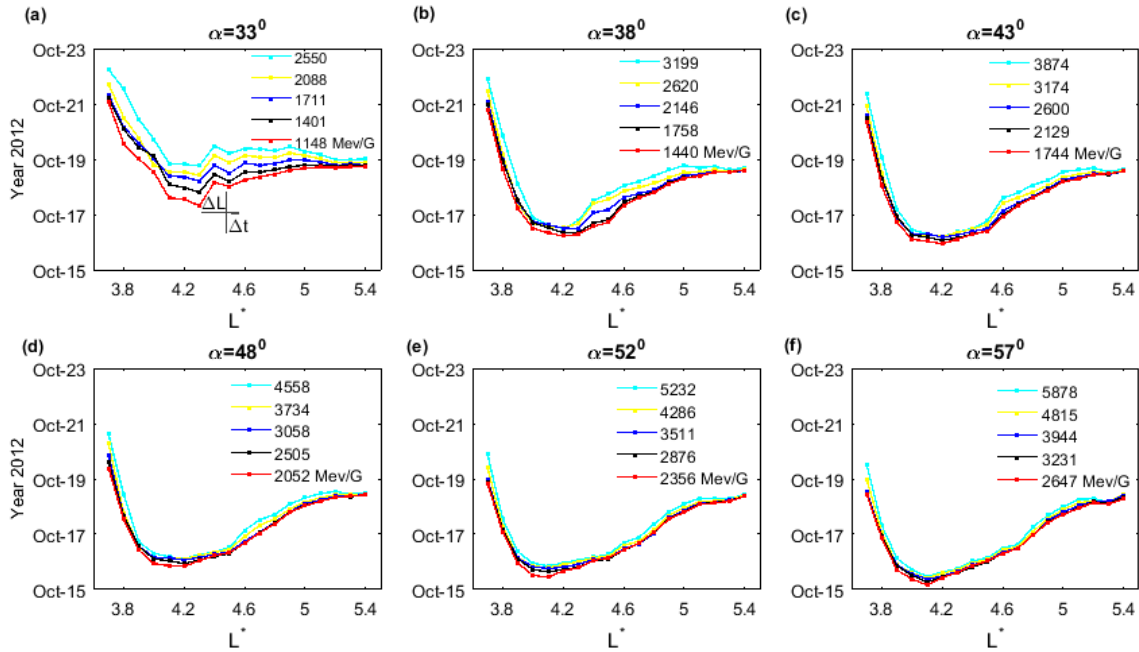
23 The panels in Figure 13 show the dependence of the maximum PSD for different values of μ
24 in the range 1148-5878 MeV/G as a function of time and L^* . The individual panels show the results
25 for different pitch angles in the range 43° to 57° . The estimates of registration time of maximum
26 PSD were made from the assimilation of REPT data from the Van Allen Probes A and B satellites.

27 As shown in Figure 13, the maximum PSD is first observed in the range $4.1 < L^* < 4.3$. and
28 has greater rate of diffusion at higher L^* compared to lower L^* for all adiabatic invariants μ and
29 pitch angles from 33° to 57° degrees. This observation is consistent with local acceleration by
30 radial diffusion and simultaneous pitch angle diffusion from high pitch angles toward loss cone.
31 For every fixed pitch angle the smaller μ , the earlier maximum PSD is observed, evidence of
32 energy diffusion source. These dependencies allow us to quantitatively estimate the radial
33 diffusion rate.

34 Figure 14 shows the same as Figure 13 except the estimates of registration time of maximum
35 PSD were made from the assimilation of MagEIS data. The dynamics of maximum PSD is shown
36 for various values of pitch angles from 43° to 57° degrees. As shown in figure, the radial diffusion
37 propagation is limited at high L^* , however injections from $L^* = 3.8$ to $L^* = 4.5$ are clearly seen.

38 Figure 15 shows the dependence of time when maximum PSD obtained from REPT
39 instruments of Van Allen Probes A and B is registered on smaller L^* from 3.4 to 3.7. Colors show
40 the dynamics of maximum PSD for different values of adiabatic invariant μ from 1148 MeV/G to
41 5878 MeV/G. The dynamics of maximum PSD is shown for various values of pitch angles from
42 33° to 57° degrees. As shown in figure, the radial diffusion rate decreases while propagating from
43 $L^* = 3.7$ to $L^* = 3.4$.

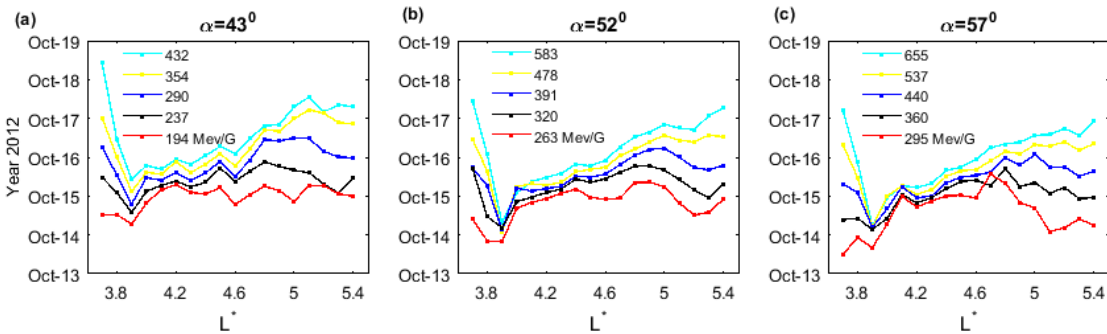
1



2

3 **Figure 13.** Dependence of time when maximum PSD is registered on L^* from 3.7 to 5.4. Colors
 4 show the dynamics of maximum PSD for different values of adiabatic invariant μ . The dynamics
 5 of maximum PSD is shown for fixed pitch angles: (a) 33° , (b) 38° , (c) 43° , (d) 48° ,
 6 (e) 52° , (f) 57° . X axis shows L^* and Y axis gives time when the PSD maximum is registered.
 7 REPT data of Van Allen Probes A and B satellites are used.

8



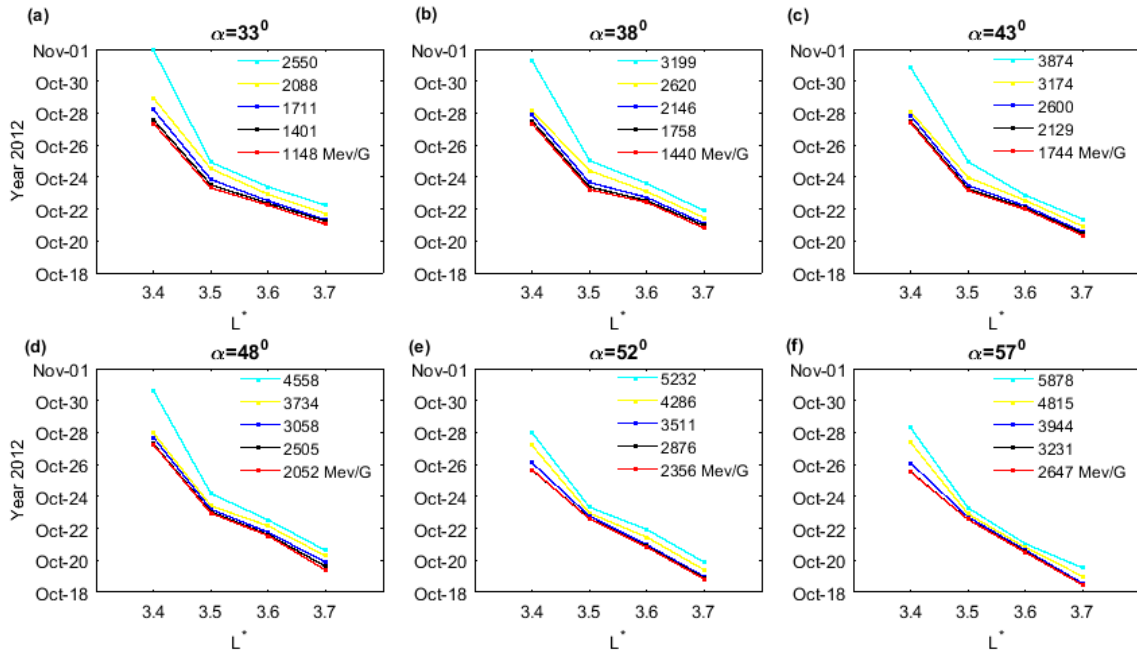
9

10 **Figure 14.** Dependence of time when maximum PSD is registered on L^* from 3.7 to 5.4. Colors
 11 show the dynamics of maximum PSD for different values of adiabatic invariant μ . The dynamics
 12 of maximum PSD is shown for fixed pitch angles: (a) 43° , (b) 52° , (c) 57° . X axis shows L^* and
 13 Y axis gives time when maximum PSD is registered. MageIS data of Van Allen Probes A and B
 14 satellites are used.

15

16 Figure 16 shows the dependence of time when the maximum PSD is registered on energy at
 17 fixed $L^* = 4.3$ RE (a) and $L^* = 4.6$ RE (b) that allows us to estimate the energy diffusion rate from
 18 experimental data. The colors show the dynamics of maximum PSD for different pitch angles from
 19 33° to 57° degrees. As shown in figure, maximum energization occurs at high pitch angles. This
 20 is consistent with energy diffusion by chorus waves. The maximum PSD is seen earlier at higher
 21 pitch angles and energy diffusion is faster at high pitch angles. The PSD maximum is also
 22 observed earlier at lower $L^* = 4.3$ compared to higher $L^* = 4.4$.

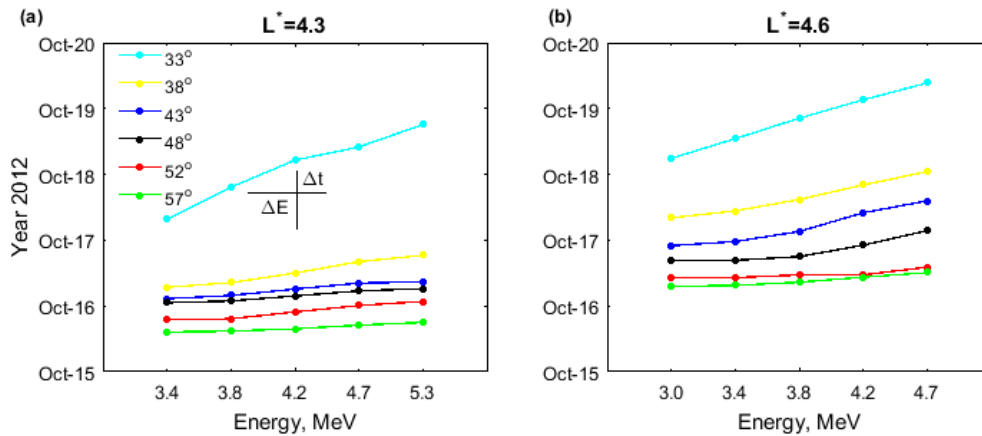
1



2

3 **Figure 15.** Dependence of time when maximum PSD is registered on L^* from 3.4 to 3.7. Colors
 4 show the dynamics of maximum PSD for different values of adiabatic invariant μ .
 5 The dynamics of maximum PSD is shown for fixed pitch angles: (a) 33° , (b) 38° , (c) 43° , (d)
 6 48° , (e) 52° , (f) 57° . X axis shows L^* and Y axis gives time when the PSD maximum is observed.
 7 REPT data of Van Allen Probes A and B satellites are used.

8



9

10

11 **Figure 16.** Dependence of time when maximum PSD is registered on energy at fixed
 12 $L^* = 4.3$ MeV (a) and $L^* = 4.6$ MeV (b). Colors show the dynamics of maximum PSD for
 13 different pitch angles from 33° to 57° . Colors show the dynamics of maximum PSD for different
 14 pitch angles: cyan - 33° , yellow - 38° , blue - 43° , black - 48° , red - 52° , and green - 57° . X
 15 axis shows energy in MeV and Y axis gives time of maximum PSD.

16

17 Figure 17 shows the dependence of time when maximum PSD is registered on pitch angle
 18 from 33° to 57° degrees at fixed energies $E \approx 3.4$ MeV (a) and $E = 3.8$ MeV (b). Colors show
 19 the dynamics of maximum PSD for different $L^* = 4.3$ (blue) and $L^* = 4.6$ (red).

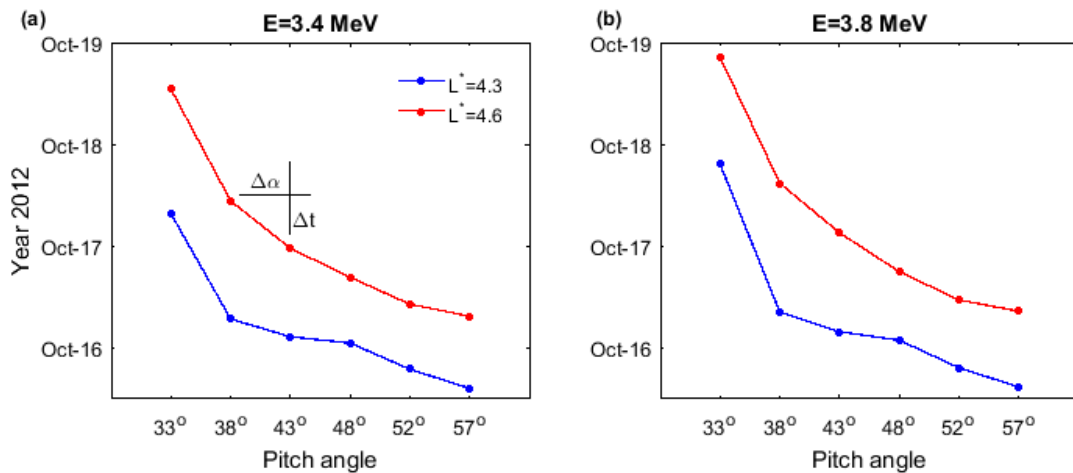


Figure 17. The dependence of time when maximum PSD is registered on pitch angle from 33° to 57° degrees at fixed energies (a) 3.4 MeV; (b) 3.8 MeV. Colors show the dynamics of maximum PSD for different $L^* = 4.3$ (blue) and $L^* = 4.6$ (red). X axis shows the pitch angles in degrees and Y axis gives time of maximum PSD.

As shown in Figure 17, the maximum PSD is registered earlier at smaller energy $E = 3.4$ MeV compared to higher energy $E = 3.8$ MeV. The pitch angle diffusion process propagates from larger to smaller pitch angles and the diffusion rate slows down with the decrease of pitch angle. This allows us to retrieve estimates of the pitch angle diffusion rate from satellite observations. This approach to extract the rates of radial, energy, and pitch angle diffusion can be developed by assimilating other events. Comparison of obtained estimates with experimental data will allow to incorporate the proper diffusion coefficients and to improve current physical models of radiation belt dynamics.

References

Brautigam, D. H., and J. M. Albert (2000), Radial diffusion analysis of outer radiation belt electrons during the October 9, 1990, magnetic storm, *J. Geophys. Res.*, 105, 291–310.

Brown R.G. Smoothing forecasting and prediction of discrete time series (1963), Prentice-HaU, N.Y., PP. 468.

Brown R.G. Smoothing forecasting and prediction of discrete time series // Prentice-HaU, N.Y. 1963. PP. 468.

Kalman, R. E. (1960), A new approach to linear filtering and prediction problems, *Trans. ASME J. Basic Eng.*, 82, 35–45.

Kalman, R. E., and R. S. Bucy (1961), New results in linear filtering and prediction theory, *Trans. ASME, Ser. D, J. Basic Eng.*, 83, 95–107.

Sage, A. P., and C. C. White (1977), *Optimum Systems Control*, 413 pp., Prentice-Hall, Upper Saddle River, N. J.